JACS
JOURNAL OF THE AMERICAN CHEMICAL SOCIETY

Article

pubs.acs.org/JACS

Imaging Excited Orbitals of Quantum Dots: Experiment and Electronic Structure Theory

Lea Nienhaus,[†,‡,∇,⊥] Joshua J. Goings,[¶,⊥] Duc Nguyen,[†,‡] Sarah Wieghold,[§] Joseph W. Lyding,[†,#] Xiaosong Li,[*,¶] and Martin Gruebele[*,†,‡,∥]

[†]Beckman Institute for Advanced Science and Technology, [‡]Department of Chemistry, [#]Department of Electrical and Computer Engineering, [∥]Department of Physics, University of Illinois, Urbana, Illinois 61801, United States

[¶]Department of Chemistry, University of Washington, Seattle, Washington 98195, United States

[§]Department of Chemistry, Technische Universität München, 85748 Garching, Germany

Supporting Information

ABSTRACT: Electronically excited orbitals play a fundamental role in chemical reactivity and spectroscopy. In nanostructures, orbital shape is diagnostic of defects that control blinking, surface carrier dynamics, and other important optoelectronic properties. We capture nanometer resolution images of electronically excited PbS quantum dots (QDs) by single molecule absorption scanning tunneling microscopy (SMA-STM). Dots with a bandgap of ∼1 eV are deposited on a transparent gold surface and optically excited with red or green light to produce hot carriers. The STM tip-enhanced laser light produces a large excited-state population, and the Stark effect allows transitions to be tuned into resonance by changing the sample voltage. Scanning the QDs under laser excitation, we were able to image electronic excitation to different angular momentum states depending on sample bias. The shapes differ from idealized S- or P-like orbitals due to imperfections of the QDs. Excitation of adjacent QD pairs reveals orbital alignment, evidence for electronic coupling between dots. Electronic structure modeling of a small PbS QD, when scaled for size, reveals Stark tuning and variation in the transition moment of different parity states, supporting the simple one-electron experimental interpretation in the hot carrier limit. The calculations highlight the sensitivity of orbital density to applied field, laser wavelength, and structural fluctuations of the QD.

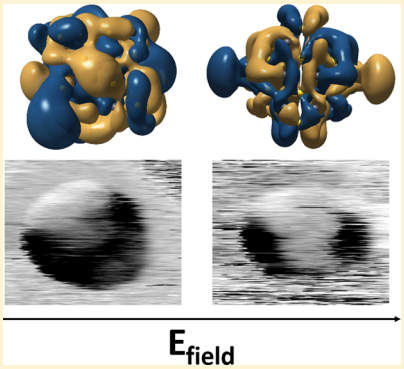

INTRODUCTION

Quantum dots (QDs) are semiconducting nanocrystals and a prototype of artificial atoms.[1−3] If the crystals are sufficiently small, their electronic properties differ strongly from the bulk material, showcasing discrete states and simple orbital shapes analogous to atoms.[4−7] The electronic structure of QDs is very important for their application as photovoltaics,[8−11] LEDs,[12−15] and FRET donors or acceptors.[16−20] In particular, high-energy excited states also are important for multicarrier properties, with applications in high efficiency light harvesting or light amplification.[21−23] Great efforts have been made to investigate the underlying electronic substructure in the broad visible absorption bands of semiconducting QDs using transient spectroscopic techniques. For example, excitons with 1 eV of excess energy can become surface trapped,[24] and at even higher energies[16] they can resemble free bulk carriers because of small scattering length.[25] Theoretical approaches including the effective mass approach[2,24,26,27] and atomistic approaches such as density functional theory (DFT)[28] have been tested, with the atomistic picture generally agreeing better with experimentally determined orbital symmetries.[26,27,29,30] Additionally, defects and surface reconstructions will require atomistic approaches such as DFT calculation.[24]

Due to their size (10^2−10^4 atoms), QDs are prone to structural or electronic defects that break the perfect symmetry present in atoms. These defects may be tailored on purpose to achieve specific optoelectronic properties, or they may be present naturally, causing problems such as fluorescence blinking when electronic excitation is trapped in surface states.[31,10] If the electronic density of excited QDs could be directly imaged, we would have a sensitive visual diagnostic of orbital symmetry and hence of presence or absence of defects. Scanning tunneling microscopy (STM) can image ground-state electron density, such as the dangling bonds on Si(100) surfaces,[32] but cannot image specific excited states. Transient or steady-state absorption spectroscopy can access specific excited states, but without the spatially resolved information on STM.

Here we combine single molecule absorption and STM (SMA-STM)[33−36] to image optical excitation of individual and paired PbS QDs. Dots deposited on a transparent conductive substrate[37] are excited by laser light. The dots are subject to a tunable electric field from the STM tip.[36] The well-studied quadratic Stark effect of QDs[38−42] allows different electronic

Received: September 1, 2015
Published: October 30, 2015

DOI: 10.1021/jacs.5b09272
J. Am. Chem. Soc. 2015, 137, 14743−14750

states to be tuned into resonance at constant laser wavelengths of 660 or 532 nm. Laser modulation results in a small tunneling current modulation that detects the difference between ground-state and excited-state electronic density of states.

We observe large shifts in the electronic density as a function of applied field, indicating a shift of different angular momentum states into and out of resonance with the laser. While some dots show a smooth excited electron density distribution indicative of few defects, others have a more complex density due to structural or electronic defects. More S- and P-like as well as irregular electron density distributions are observed. We also observe orbital alignment of adjacent QDs, an indication that interdot electronic coupling may be present.

We complement the experiments with electronic structure calculations on a small PbS model QD, inspired by recent work on ZnO QDs.[6] Adding an electric field to the calculations, suitably scaled to take into account the smaller polarizability of the smaller model QD, reveals strong quadratic Stark tuning of the energy levels. Red shifts at field strengths comparable to experiment indeed bring different angular momentum excited states into resonance at a given frequency. Thus, a combination of excitation wavelength, electric field, and proximity of QDs can be used to switch their electronic structure and tune their interactions, and such switching and tuning can now be visualized directly.

MATERIALS AND METHODS

Transparent Substrate Preparation for SMA-STM. We illuminate the sample from the rear to avoid tip heating.[33−37] Transparent 15 nm high gold-on-platinum films are fabricated by electron beam evaporation onto annealed c-plane sapphire substrates as previously reported.[37] These films have large (>100 nm) atomically flat regions separated by step edges. Thick silver contacts are painted onto the sample edges with colloidal silver paint (TedPella Inc.) to improve contact between the ultrathin film and the sample holder. A total internal reflection geometry is obtained by attaching a 3 mm fused silica right angle prism (Thorlabs) to the sapphire backside of the sample, using a UHV compatible epoxy (302−3M, Epotek). The perpendicular transmission of the metal film on sapphire is ca. 25%, and an additional ca. 20% of light is lost at the vacuum−prism and prism−epoxy−sapphire interface. Prior to STM imaging, the sample undergoes an elevated temperature degas at 120 °C for 12 h.

Transfer of PbS Quantum Dots to the Substrate. PbS QDs (available from Evident Thermoelectrics) have a nominal diameter of 4.2 nm and molecular mass 34 kDa excluding oleic acid ligands. The first absorption peak lies at 1228 nm and the emission peak at 1315 nm. Two methods are used to deposit dots onto the transparent gold substrate. Dry contact transfer (DCT)[43] is used with a modification: to overcome QD aggregation, carbon nanotubes (CNTs) are used as a deposition matrix. The DCT applicators containing a piece of frayed fiberglass tied onto a tip holder are loaded with CNTs by rubbing onto the CNT powder. After that, three drops of the PbS QD solution (1.0 mg/mL in toluene) are added. The applicators are then degassed overnight by gentle resistive heating, keeping the pressure below 10^{-8} Torr at all times, and without affecting dot fluorescence.[44] QDs are also deposited on the surface by an aerosol method. For aerosol deposition, the PbS QD stock solution (10 mg/mL) is diluted: 5 μL is added to 1 mL of toluene. An Iwata SM-SB airbrush is filled with 200 μL of the diluted QD solution. The solution is repeatedly pulsed on the sample at a distance of 10 cm, while allowing the sample to fully dry between pulses. Similar data are obtained both ways.

SMA-STM Setup. STM imaging is performed on a home-built UHV STM similar to ones previously reported.[32] SMA-STM images were taken with mechanically cut Pt−Ir (80:20) tips at a typical current of 5 pA and variable sample bias. For SMA-STM, the laser enters through a fused silica prism on the back of the sapphire substrate and propagates to the Pt−Au film at the front. Total internal reflection results in an evanescent wave at the tip−sample junction, which excites the chromophores on the gold film.[35] The sample is illuminated from behind by a 532 nm diode pumped solid-state (DPSS) laser at an excitation power of ca. 1250 mW/mm^2. Amplitude modulation of the laser by means of a chopper wheel at a frequency of 2.2 kHz allows for simultaneous detection of the topographic STM image and the in-phase (X) and 90° out-of-phase (Y) images of the current modulation detected by lock-in amplifier (Stanford Research ST830). The lasers are p-polarized (in the plane of incidence).

For comparison of different excitation wavelengths, a 660 nm diode laser is sent through the chopper wheel 180° phase shifted to the 532 nm DPSS laser, and the resulting modulated beams are co-aligned. For optimal comparison of the resulting SMA-STM signal, similar excitation power densities are necessary. To compensate for the higher absorption in the film[45] and a larger spot size, we require a ca. 4 times higher power at 660 nm than at 532 nm. To accomplish this, the power density at 532 nm is lowered to ca. 350 mW/mm^2.

The oscillator strength in the strong confinement limit (<10 nm for PbS)[46] is about (10 nm/4.2 nm)^3 ≈ 13.5 times larger for our QDs than for bulk excitons. The extinction coefficient is about 3 times larger at 532 nm than near the bandgap (see below for discussion of the calculation). In addition, enhancement factors $f^2 \approx 1000$ for the laser intensity have been shown near metal tips.[35,47] Even with subpicosecond carrier relaxation times τ_r expected for more highly excited states due to intraband phonon relaxation,[48−50] our laser intensity I is sufficient to saturate the electronic excitation, using the equation $I_{saturation} = (2\sqrt{2}hc)/(f^2\pi\tau_r\lambda^3)$.[35] At lower laser intensity or for the very fastest relaxation processes, the images may also contain contributions from relaxed electronic states closer to the bandgap or even phonons (nanoscale heating following absorption). While the laser is on for ca. 450 μs and $I \geq I_{saturation}$, the electron density is the average of the excited- and ground-state densities. When the laser is off and $I = 0$, the electron density is the ground-state density. Thus, with the laser modulated on−off much more slowly than the relaxation time, the tunneling current modulation detected by the lock-in amplifier approximately images the difference of ground and excited local electron densities.

Computational Methods. As a naïve one-electron orbital picture in Figure 1, we used 1S and 1P states of a particle in a sphere, calculated the density difference to simulate the experimental difference of ground-state and excited-state local electron densities, and projected the density difference into two dimensions, as mapped by STM. This approach shows what types of difference signals could show up in the experiment for different parity orbitals, although it should not be taken as a quantitative description of the data.

To investigate orbital structure at a much higher level, DFT calculations are performed using the development version of the Gaussian program.[52] PbS QD structures are computed using the PBE1PBE hybrid DFT functional,[53,54] with the Los Alamos double-ζ pseudocore potential (LANL2DZ) and associated basis set with additional polarization functions.[55−58] Cubic PbS QDs are constructed with a principal diagonal of 1.495 nm (see Figure S1 for the exact structure used). In accordance with previous literature reports, the cubic PbS QDs are constructed in stoichiometric ratios, which was shown to result in a semiconducting behavior with no midgap states.[59] To account for the tunable static field from the STM tip, a finite electric field is applied along a face of the PbS QD cubes, and five electronic structures are computed ranging from 0 to 1.8 V/nm (see Figure S2 for the electronic structure at 1.8 V/nm). At each field, the QD structure is relaxed to an optimized geometry.

A simulated absorption spectrum is generated from the computed transition moments between occupied and unoccupied DFT orbitals and their energy differences. To match experimental values approximately, the computed energies are scaled by the ratio of the computed and experimental band gap energies (3.022 vs 1.010 eV). Each peak in the computed spectra was dressed with a Gaussian function with a broadening constant of 0.016 eV. Orbital reflection parity is determined (fixing the axis of symmetry parallel to the applied static electric field) by generating a series of 10,000 random points in

DOI: 10.1021/jacs.5b09272
J. Am. Chem. Soc. 2015, 137, 14743−14750

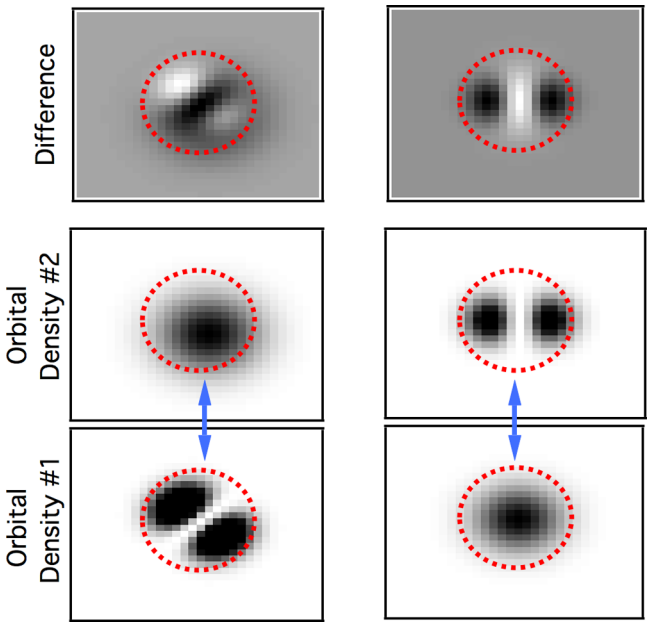

Figure 1. Schematic orbital electron density differences for the one-electron particle in a box picture. Left column: density difference (top) resulting from transition connecting a near-even parity but displaced (S-like) orbital and a rotated odd parity (P-like) orbital. The displacement of the S-like orbital is meant to simulate a loss of perfect spherical symmetry due to a surface defect. Right column: density difference (top) resulting from transition connecting perfect odd (P-like) and even (S-like) orbital. The blue arrows indicate Rabi cycling between orbitals at high laser intensity. The calculation of the schematic picture is described in Materials and Methods.

the orbital density, reflecting through the symmetry axis, and determining the sign change. If the odd or even parity is >70% of the total number of points tested, the parity is assigned. For computationally inconclusive parity assignments, parity is assigned by inspection. For orbital plots, an ISO value of 0.004 is used. This value gave the best compromise of overall long-range shape vs short-range atomic electron density. Figure S3 demonstrates the effect of picking different ISO values on the appearance of one of the orbitals visualized for this study.

RESULTS AND DISCUSSION

We excited ca. 4.2 nm diameter PbS QDs deposited on a transparent gold layer. When the optical transition is saturated, the SMA-STM signal is approximately proportional to the difference between excited- and ground-state local electron densities (see Materials and Methods). Only near the band gap does excitation occur from well-defined S- to P-like states.[46] For excitation from lower lying occupied molecular orbitals (OMOs) to higher lying unoccupied molecular orbitals (UMOs), we can still usefully classify transitions by parity, e.g., +/−. Figure 1 illustrates a naïve one-electron particle-in-a-box picture for laser cycling between different parity states and what the density differences look like projected in 2-D (see Materials and Methods). The offset S-like density on the left is meant to simulate the influence of a defect on a perfect S symmetry, shifting the charge distribution nearer the surface on one side of the dot.

Single Quantum Dot Experiments. The top row in Figure 2b shows the change in the 532 nm absorption images for an isolated PbS QD when the applied electric field is increased from 0.8 V sample bias (≈0.47 V/nm) to 2.0 V (≈0.97 V/nm). For reference, two one-electron, particle-in-a-sphere density differences from Figure 1 are shown above the experimental data in Figure 2a. In the case of a positive bias, electrons tunnel from the tip to sample UMOs. Different excited states are tuned into resonance at the different fields. At 0.8 V the signal (black) fills a bar near the center of the QD. When the applied bias is increased, the signal becomes localized on one side of the QD in a "C" shape. Finally at 2.0 V bias, the signal is largest in two lobes on the opposite sides of the QD and smallest in-between. The experimental images can be compared roughly with the density differences in Figure 1, reproduced for convenience in Figure 2a, although the angular momenta of the excited states imaged experimentally in Figure 2b are probably >1. Figures S4 and S5 show additional SMA-STM images at different biases, and the corresponding out-of-phase lock-in amplifier images show that the signal occurs at the correct phase with respect to the laser modulation (instant response as opposed to delayed response due to thermal effects).

The bottom row in Figure 2b shows the same QD at the same electric fields, but at a reversed sample bias ranging from −1.5 to −0.8 V. In that case, electron tunneling from the sample to the tip occurs, and OMOs are imaged. A similar trend is observed, but the trend also reveals differences between the UMO and OMO state's local electronic density. At −1.5 V, the signal already shows separate lobes, while at +1.5 V we still observe a C-shaped absorption signal. Noteworthy is that the signal maximum appears at a different absolute value for positive (black) and negative (white) bias. At positive bias, the "signal maximum", when the QD is filled in the most, is at ≈1.2 V, while at negative bias, this signal maximum appears at about ≈−0.8 V (see SI). Thus, local maxima in the oscillator strength are accessed at slightly different Stark shifts in the two cases. A linear offset of the quadratic Stark shift could also contribute to the observed asymmetry.[38,60]

The 180° phase shift of the absorption signal (black to white), observed when going from positive to negative bias, is easily explained by the tunneling direction. When a positive bias is applied to the sample, the electrons tunnel from the tip to surface. Hence we are imaging unfilled states (UMOs). Laser excitation populates the UMOs and results in a decreased tunneling current due to the lowered tunneling probability from tip to surface via the filled ground-state UMOs (black signal in Figure 2b). Reversing the bias to negative values results in tunneling from the surface to the tip. Here we are imaging the electrons tunneling from the OMOs. Absorption facilitates tunneling from OMOs and results in an increased tunneling current (white signal in Figure 2b).

The integrated signal strength observed at positive bias is generally higher than the signal strength at negative bias. Such asymmetry can be caused by net rectification of the optical field. Rectification effects have been observed in the case of surface plasmons and also for electron transfer between the HOMO and LUMO of a donor and acceptor.[61−63] In our case, rectification could be caused by tip−surface asymmetry, not necessarily by the QD itself, and our laser accesses highly excited states, not the HOMO/LUMO bandgap region at ≈1200 nm.

To verify that the absorption signal remains aligned with the surface and laser polarization geometry, but not with the tip scan direction, we also scanned the tip in different directions over the same QD (Figure S6). The SMA-STM image showed no signs of realigning with the scan direction and is a fixed feature of the laser polarization and geometry of the QDs on

DOI: 10.1021/jacs.5b09272
J. Am. Chem. Soc. 2015, 137, 14743−14750

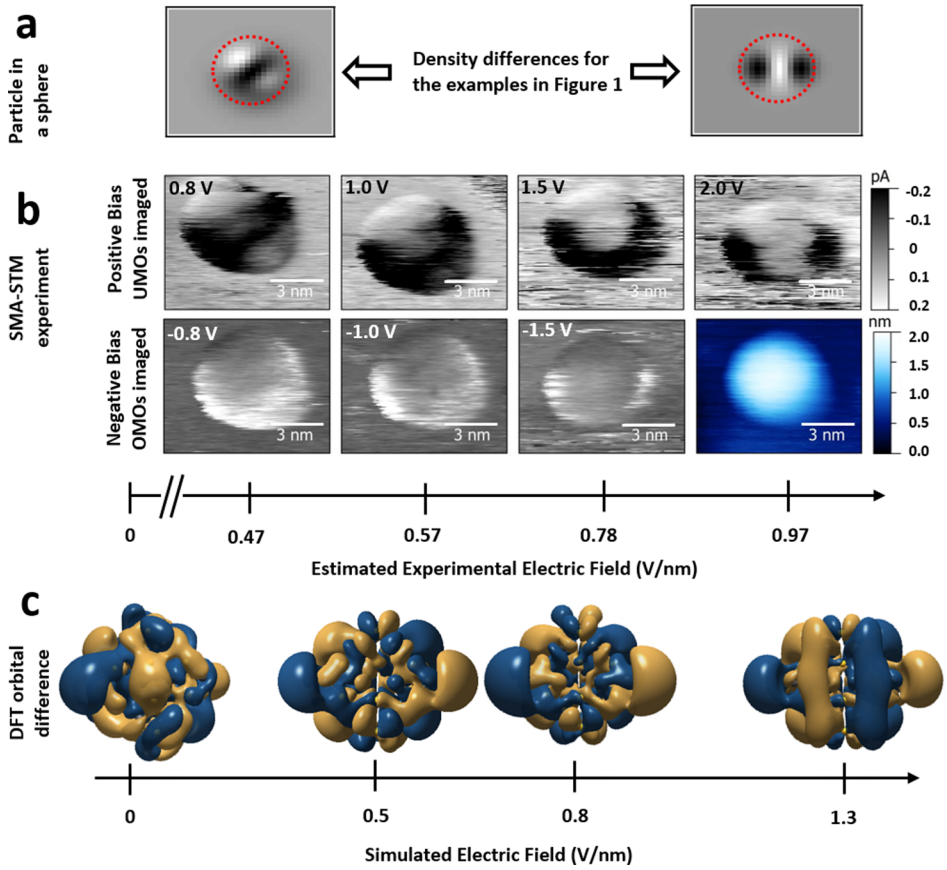

Figure 2. (a) Electron density differences for the examples in Figure 1, reproduced for direct comparison with (b). (b) SMA-STM images of a single PbS QD under 532 nm illumination. The dot was deposited by DCT on the atomically flat gold surface. Top row: phase-optimized absorption signal as a function of electric field at a positive tunneling bias. Bottom row: same dot at negative tunneling bias; a topography image collected at −1 V is shown in the blue inset. The *x*-axis shows the estimated absolute experimental electric field value based on the tip−sample distance of ca. 1.9 nm. Tunneling current: 10 pA. (c) DFT orbital density difference at constant excitation energy and increasing field, taken as the point-wise difference of the UMO versus OMO. A scaled excitation energy of about 2.35 eV was used for comparison with experiment. The applied field is perpendicular to the plane of the page, like the major field component in the experiment. As in the experiment, a trend from more uniform to more left−right polarized density difference is observed in the calculations, although the experimental asymmetry cannot be reproduced unless the PbS lattice is displaced in the calculations (see Figure 7 which shows an asymmetric simulated signal).

the surface. Thus, the tip field, which has a ca. 10−20% lateral component depending on tip position near the QD, is relatively uniform when the tip is in proximity of the QD.

For some isolated QDs, the excitation image remains irregularly shaped at all fields we can access (Figure 2). For others the signal, which projects electronic density modulation into the sample plane, has nearly perfect spherical symmetry (Figure 3, top dot and ref 37). At the spatial resolution of our topography scans (rightmost image in the bottom row of Figure 2b), we cannot determine whether the irregular shape of the orbital we image is due to electronic defects (e.g., pinned charges, dopant atoms) or due to an irregularly shaped surface (e.g., missing atom at a terrace edge).

Quantum Dot Pair Excitation and Wavelength Dependence. Another interesting result in Figure 3 is the excited-state−ground-state density difference observed in an anisotropic local environment. The two PbS QDs at the bottom are in direct contact. In contrast to the single dot at the top, they show an electron density difference between the ground and excited states characteristic of higher angular momentum orbitals (e.g., P) at 532 nm excitation. The two excitations are aligned perpendicular to the center-to-center axis of the two QDs. If two nanoparticles are in close proximity, coupling

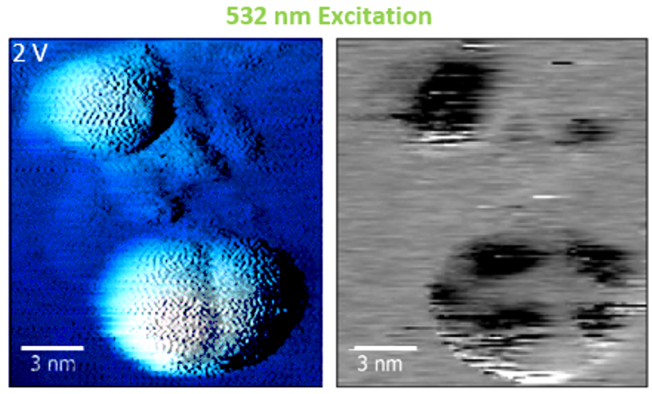

Figure 3. SMA-STM image of PbS QDs deposited by aerosol deposition onto a Pt−Au surface. For enhanced contrast of the adjacent QDs, the topograph (left) was overlaid with the topographic derivative (compare Figure S7). The in phase lock-in image (right) shows a different absorption signal for a single QD as for two adjacent QDs. The single QD (same as ref 37, Figure 7) shows S-type behavior, while the two dots at the bottom feature aligned higher angular momentum excitations. Scanning conditions: 5 pA, 2 V. Color scale for lock-in image (right): −0.2 pA (black), 0.2 pA (white).

DOI: 10.1021/jacs.5b09272
J. Am. Chem. Soc. 2015, 137, 14743−14750

between nearly resonant energy levels can orient their wave functions and shift energies to bring different states into resonance with the optical excitation.[64−66] The resulting symmetric and antisymmetric combinations are analogs of bonding and antibonding orbitals between a pair of atoms. The electron density difference in Figure 3 is consistent with such coupling, but not proof. So far, we have not been able to manipulate dots while imaging them under laser illumination to see if the alignment is broken at a larger distance between dots.

Thus far we have tuned different excited states into resonance by using the quadratic Stark effect at a single wavelength. Figure 4 illustrates that we can observe similar

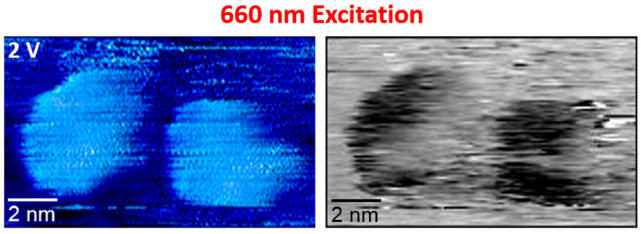

Figure 4. Topograph image overlaid with the topographic derivative for enhanced contrast (left) of two more QDs with the corresponding in-phase lock-in amplifier image (right), showing P-type signals. Dots were deposited by DCT. Scanning conditions: 660 nm excitation, 5 pA, 2 V. Color scale for lock-in image (right): −0.2 pA (black), 0.2 pA (white).

signals at a different excitation wavelength. The SMA-STM signal excited at 660 nm and a high field shows a clear two-lobed signal on the right QD (e.g., +/− parity transition), analogous to 532 nm excitation, and a more asymmetrical orbital density difference on the left QD. Additional images for the same dots at 532 and 660 nm excitation subject to different electric fields are seen in Figure S8. The comparison of 532 nm excitation at lower electric field and 660 nm excitation at higher field in Figure S8 shows that it is possible to access orbitals with a range of electron density distributions and alignments in the case of adjacent QDs.

Computational Results. To check whether it makes sense to interpret our images in terms of Stark-shifted orbitals and a naïve one-electron/hole picture in Figure 1, as suggested by high excess energy ultrafast laser experiments,[25] we performed electronic structure calculations of a small model PbS QD in an electric field. Figure S1 shows the structure of the 1.5 nm diameter model dot. The driving force for changes in orbital energy and shape in SMA-STM experiments is the tunable Stark shift of the orbitals in the PbS QD. A plot of the orbital energies as a function of field strength is given in Figure 5. The orbitals are normalized such that the HOMO (Fermi level) has zero energy. As the applied field increases, the band gap narrows. Most higher energy orbitals shift to lower energy also. Levels become nondegenerate, and at higher fields entire bands cross and mix (e.g., states around 6.0 eV at a field strength of 1 V/nm).

Figure 6 shows calculated absorption spectra of the model PbS dot. The energy axis has been scaled down by a factor of 3.066 from the original calculation to match up calculated and experimental band gaps. As the field strength increases, the peaks in the absorption spectrum shift in energy as well as oscillator strength. How the peaks shift depends on the exact nature of the transition. Since the experiments show excitation images corresponding to different parities, the simulated

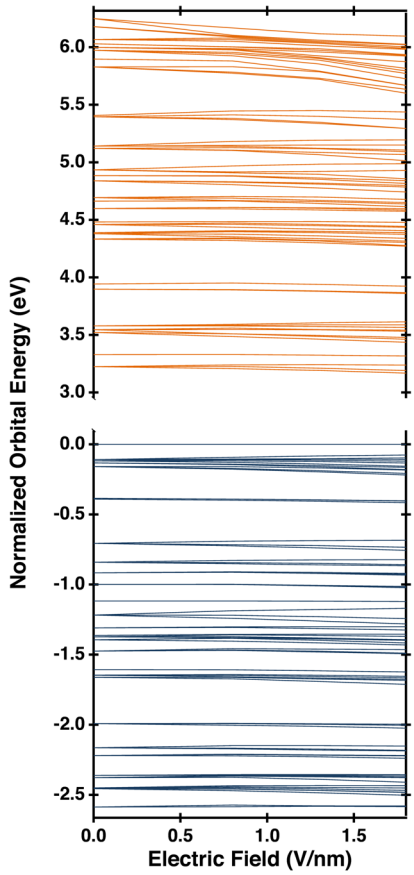

Figure 5. Plot of orbital energy levels as a function of field strength. The orbitals are normalized such that the HOMO (Fermi level) has zero energy. As the applied field increases, the fundamental band gap narrows and other levels split and cross at higher fields.

spectrum was decomposed according to parity (reflection symmetry through an arbitrary plane parallel to the applied field). Figure 6 shows only the even to odd and even to even transitions. Other parity combinations are given in the Figures S9 and S10. Experimentally, the observed QD absorption continues to increase well above the band gap threshold. In the simulated spectrum, the increase stops above 2.4 eV because of the finite basis in the DFT calculations. Such highly excited states could be described by adding additional diffuse functions, albeit at increased computational cost.

In the SMA-STM experiment the QDs are illuminated with 2.33 eV (532 nm) light. In Figure 6, the inset highlights this region of the simulated and energy-scaled spectra. As the field increases, different parity peaks red-shift and dip in intensity by different amounts: The even to odd transition red-shifts faster than the even to even transition. Assuming we are looking down the z-axis, an even to odd transition corresponds to an S to P_x- or P_y-like transition; an even to even transition corresponds to either a P_z- to S-like or S- to P_z-like transition (or similar parity changes with higher angular momentum).

Plots of the calculated electronic transition orbitals give further evidence of Stark tuning. An orbital difference for one of the more intense peaks in the region 2.25 to 2.45 eV is shown in Figure 2c, for easy comparison with experiment. As the field tunes over the 1 V/nm range, the transition orbital changes from a more uniform density difference to one that becomes left−right lobed, in analogy to the progression of difference density observed experimentally in Figure 2a. Of course the

DOI: 10.1021/jacs.5b09272
J. Am. Chem. Soc. 2015, 137, 14743−14750

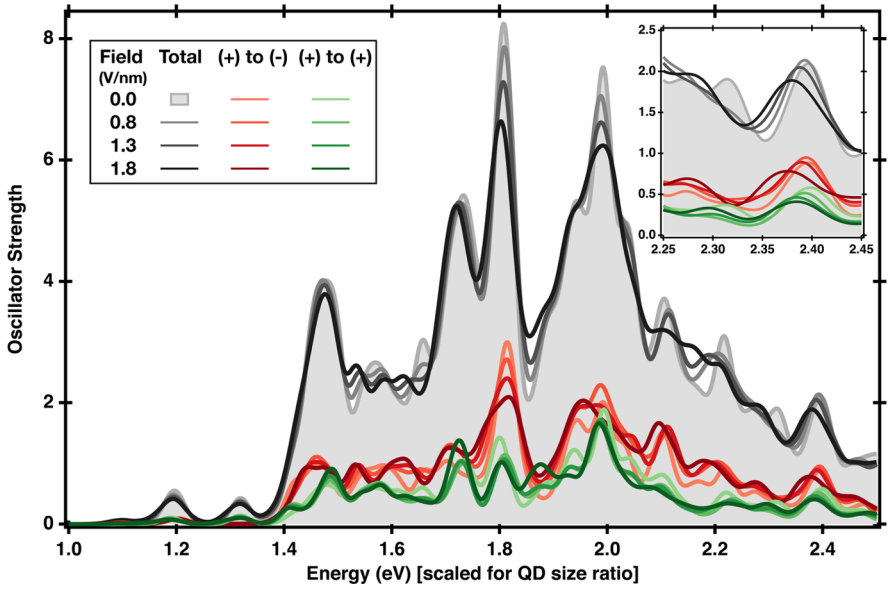

Figure 6. The effect of an increasing static field on the absorption spectra of the simulated PbS QD. As the field strength increases, the peaks in the absorption spectrum shift in energy as well as oscillator strength. The inset shows the simulated spectra near the experimental excitation energy of 2.33 eV.

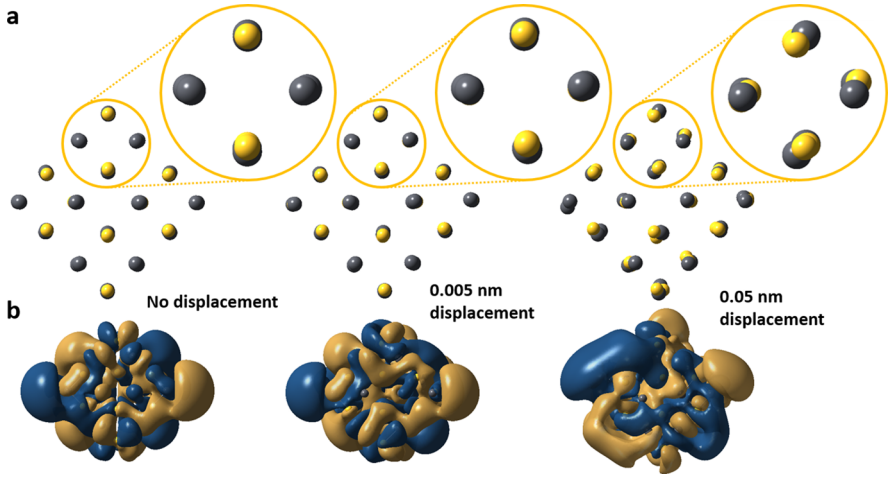

Figure 7. Comparison of the symmetrized orbital at 0.5 V/nm and ≈2.35 eV in Figure 2c with a calculation where the atoms were randomly displaced by 0.005 and 0.05 nm. (a) The lattice with a zoomed in area to highlight the displacement. (b) Represents the orbitals.

simulation on a symmetric crystal cannot reproduce the asymmetry seen in the middle panels of the experimental Stark tuning progression. The smaller simulated QD is less polarizable,[38] and generally larger field changes are required in order to shift the character of the resonant orbital appreciably ($\Delta E \sim 1$ V/nm in the calculation vs ~0.25 V/nm experimentally). With the caveat that the rate of Stark tuning is smaller for the simulated dot and that the experimental dots have defects, the calculations suggest that the one-electron picture is a reasonable first approximation.

Although some of the experimental dots have nearly symmetric density differences (e.g., Figure 3), most transitions that we observed do not have a symmetrical density (e.g., the "C" shape in Figure 2b). To see whether simulations could account for such an observed loss of symmetry, we compared the symmetrized orbital at 0.5 V/nm and ≈2.35 eV in Figure 2c with a calculation where the atoms were randomly displaced by 0.005 and 0.05 nm. The plots are shown in Figure 7. For the QD with atoms displaced by 0.005 nm, the transition looks very similar to the undisplaced QD reference. While some symmetry is lost, the 0.005 nm displaced QD largely retains the P-like excited-state density. This is a qualitative confirmation of the robustness of the calculations, as the excited-state density is stable to small geometric perturbations. However, defects can remove, substitute, or add entire atoms, so we also investigated the same QD transition and field with 0.05 nm displacements, more comparable to atomic size. Here the excited-state density is largely deformed, and the P-like shape of the electronic transition is lost. Thus, it is plausible that large perturbations from a perfect geometry can give rise to the deformed orbital density differences observed experimentally in Figures 2b and 3.

CONCLUSIONS

Electronic nanostructures are difficult to control at the atom-by-atom level, as is also true for very large molecules. Even the highest fidelity copying processes known at the molecular level, DNA-RNA transcription or RNA-protein translation, produce a distribution of molecules when the RNAs or proteins are large

DOI: 10.1021/jacs.5b09272
J. Am. Chem. Soc. 2015, 137, 14743−14750

enough. The question is how well nanostructures or molecules can still function under such conditions and how errors can be diagnosed. Here we demonstrated that we can image electronic transition density differences in QDs, as a diagnostic of the orbital shapes involved in the transition. Both laser wavelength and Stark tuning were used to bring different transitions in a PbS QD into resonance and image the corresponding electronic density differences. We found cases where the signal is nearly symmetric, others where it becomes localized, and also cases where orbitals align in closely paired QDs deposited on a gold surface. While electronic structure calculations on a small model dot (1.5 vs 4.2 nm in experiment) cannot be quantitatively matched with experiment, they show all the same features: the contribution of different parity states to the signal changes as the electric field is tuned, or the wavelength is changed; the magnitude of the field required tune orbitals is somewhat larger than experiment, in keeping with the smaller polarizability of the model. And deforming the model on a length scale of atom-size defects produces large changes and loss of symmetry in the transition difference orbitals, in analogy to the asymmetric electron density differences observed in the experiment. Thus, SMA-STM can directly visualize electronic structure shape changes characteristic of structural defects, going beyond spectral intensities or energy/time responses. It may even become possible in the near future to deform QDs with a tip, diagnose their excited states, and shape them to have desirable electronic properties.

■ ASSOCIATED CONTENT

Supporting Information

The Supporting Information is available free of charge on the ACS Publications website at DOI: 10.1021/jacs.5b09272.

Additional details of the experimental measurements, STM images, electronic structure calculations, dot geometry and energy values (PDF)

■ AUTHOR INFORMATION

Corresponding Authors

*xsli@uw.edu

*mgruebel@illinois.edu

Present Address

[▽]Department of Chemistry, Massachusetts Institute of Technology, 77 Massachusetts Ave. Building 2−216, Cambridge, Massachusetts, 02139, United States

Author Contributions

[⊥]These authors contributed equally.

Notes

The authors declare no competing financial interest.

■ ACKNOWLEDGMENTS

The authors thank Stevia Angesty for early development of the aerosol deposition technique used for some of the images obtained here. The work at Illinois was supported by a grant from the National Science Foundation, NSF CHE 1307002 (L.N., D.N., S.W., J.L., M.G.). E-beam evaporation was carried out at the Micro and Nanotechnology Laboratory, University of Illinois. The computational work at the University of Washington was supported by a U.S. National Science Foundation Graduate Research Fellowship (DGE 1256082 to J.J.G.) and grants from the National Science Foundation, NSF CHE 1265945 and DMR 1408617 (J.J.G. and X.L.)

■ REFERENCES

(1) Choi, C. L.; Alivisatos, A. P. *Annu. Rev. Phys. Chem.* **2010**, *61*, 369.

(2) Norris, D. J.; Bawendi, M. G. *Phys. Rev. B: Condens. Matter Mater. Phys.* **1996**, *53*, 16338.

(3) Mahadevu, R.; Pandey, A. *J. Phys. Chem. C* **2014**, *118*, 30101.

(4) Cui, J.; Beyler, A. P.; Bischof, T. S.; Wilson, M. W. B.; Bawendi, M. G. *Chem. Soc. Rev.* **2014**, *43*, 1287.

(5) Bawendi, M. G.; Steigerwald, M. L.; Brus, L. E. *Annu. Rev. Phys. Chem.* **1990**, *41*, 477.

(6) Goings, J. J.; Schimpf, A. M.; May, J. W.; Johns, R. W.; Gamelin, D. R.; Li, X. *J. Phys. Chem. C* **2014**, *118*, 26584.

(7) Roest, A. L.; Germeau, A.; Kelly, J. J.; Vanmaekelbergh, D.; Allan, G.; Meulenkamp, E. A. *ChemPhysChem* **2003**, *4*, 959.

(8) Chuang, C.-H. M.; Brown, P. R.; Bulović, V.; Bawendi, M. G. *Nat. Mater.* **2014**, *13*, 796.

(9) Tang, J.; Kemp, K. W.; Hoogland, S.; Jeong, K. S.; Liu, H.; Levina, L.; Furukawa, M.; Wang, X.; Debnath, R.; Cha, D.; Chou, K. W.; Fischer, A.; Amassian, A.; Asbury, J. B.; Sargent, E. H. *Nat. Mater.* **2011**, *10*, 765.

(10) Kamat, P. V. *J. Phys. Chem. C* **2008**, *112*, 18737.

(11) Semonin, O. E.; Luther, J. M.; Choi, S.; Chen, H.-Y.; Gao, J.; Nozik, A. J.; Beard, M. C. *Science* **2011**, *334*, 1530.

(12) Anikeeva, P. O.; Halpert, J. E.; Bawendi, M. G.; Bulović, V. *Nano Lett.* **2009**, *9*, 2532.

(13) Caruge, J. M.; Halpert, J. E.; Wood, V.; Bulovic, V.; Bawendi, M. G. *Nat. Photonics* **2008**, *2*, 247.

(14) Anikeeva, P. O.; Halpert, J. E.; Bawendi, M. G.; Bulović, V. *Nano Lett.* **2007**, *7*, 2196.

(15) Supran, G. J.; Song, K. W.; Hwang, G. W.; Correa, R. E.; Scherer, J.; Dauler, E. A.; Shirasaki, Y.; Bawendi, M. G.; Bulović, V. *Adv. Mater.* **2015**, *27*, 1437.

(16) Kagan, C. R.; Murray, C. B.; Nirmal, M.; Bawendi, M. G. *Phys. Rev. Lett.* **1996**, *76*, 1517.

(17) Clapp, A. R.; Medintz, I. L.; Mauro, J. M.; Fisher, B. R.; Bawendi, M. G.; Mattoussi, H. *J. Am. Chem. Soc.* **2004**, *126*, 301.

(18) Clapp, A. R.; Medintz, I. L.; Mattoussi, H. *ChemPhysChem* **2006**, *7*, 47.

(19) Suzuki, M.; Husimi, Y.; Komatsu, H.; Suzuki, K.; Douglas, K. T. *J. Am. Chem. Soc.* **2008**, *130*, 5720.

(20) Algar, W. R.; Wegner, D.; Huston, A. L.; Blanco-Canosa, J. B.; Stewart, M. H.; Armstrong, A.; Dawson, P. E.; Hildebrandt, N.; Medintz, I. L. *J. Am. Chem. Soc.* **2012**, *134*, 1876.

(21) Nozik, A. J. *Phys. E* **2002**, *14*, 115.

(22) Konstantatos, G.; Howard, I.; Fischer, A.; Hoogland, S.; Clifford, J.; Klem, E.; Levina, L.; Sargent, E. H. *Nature* **2006**, *442*, 180.

(23) Klimov, V. I.; Mikhailovsky, A. A.; McBranch, D. W.; Leatherdale, C. A.; Bawendi, M. G. *Science* **2000**, *287*, 1011.

(24) Tyagi, P.; Cooney, R. R.; Sewall, S. L.; Sagar, D. M.; Saari, J. I.; Kambhampati, P. *Nano Lett.* **2010**, *10*, 3062.

(25) Cho, B.; Peters, W. K.; Hill, R. J.; Courtney, T. L.; Jonas, D. M. *Nano Lett.* **2010**, *10*, 2498.

(26) Kambhampati, P. *Acc. Chem. Res.* **2011**, *44*, 1.

(27) Sewall, S. L.; Cooney, R. R.; Kambhampati, P. *Appl. Phys. Lett.* **2009**, *94*, 243116.

(28) Wang; Zunger, A. *J. Phys. Chem. B* **1998**, *102*, 6449.

(29) Fu, H.; Wang, L.-W.; Zunger, A. *Appl. Phys. Lett.* **1997**, *71*, 3433.

(30) Efros, A. L.; Rosen, M. *Appl. Phys. Lett.* **1998**, *73*, 1155.

(31) Galland, C.; Ghosh, Y.; Steinbruck, A.; Sykora, M.; Hollingsworth, J. A.; Klimov, V. I.; Htoon, H. *Nature* **2011**, *479*, 203.

(32) Lyding, J. W.; Shen, T. C.; Hubacek, J. S.; Tucker, J. R.; Abeln, G. C. *Appl. Phys. Lett.* **1994**, *64*, 2010.

(33) Ballard, J.; Carmichael, E.; Lyding, J.; Gruebele, M. *Nano Lett.* **2006**, *6*, 45.

(34) Scott, G.; Ashtekar, S.; Lyding, J.; Gruebele, M. *Nano Lett.* **2010**, *10*, 4897.

(35) Carmichael, E. S.; Ballard, J. B.; Lyding, J. W.; Gruebele, M. *J. Phys. Chem. C* **2007**, *111*, 3314.

(36) Nienhaus, L.; Wieghold, S.; Nguyen, D.; Lyding, J.; Scott, G. E.; Gruebele, M. *ACS Nano* **2015**, DOI: 10.1021/acsnano.5b04872.

(37) Nienhaus, L.; Scott, G. E.; Haasch, R. T.; Wieghold, S.; Lyding, J.; Gruebele, M. *J. Phys. Chem. C* **2014**, *118*, 13196.
(38) Empedocles, S. A.; Bawendi, M. G. *Science* **1997**, *278*, 2114.
(39) Brus, L. *Appl. Phys. A: Solids Surf.* **1991**, *53*, 465.
(40) Seufert, J.; Obert, M.; Scheibner, M.; Gippius, N. A.; Bacher, G.; Forchel, A.; Passow, T.; Leonardi, K.; Hommel, D. *Appl. Phys. Lett.* **2001**, *79*, 1033.
(41) Unold, T.; Mueller, K.; Lienau, C.; Elsaesser, T.; Wieck, A. D. *Phys. Rev. Lett.* **2004**, *92*, 157401.
(42) Park, K.; Deutsch, Z.; Li, J. J.; Oron, D.; Weiss, S. *ACS Nano* **2012**, *6*, 10013.
(43) Albrecht, P. M.; Lyding, J. W. *Appl. Phys. Lett.* **2003**, *83*, 5029.
(44) Jarosz, M. V.; Porter, V. J.; Fisher, B. R.; Kastner, M. A.; Bawendi, M. G. *Phys. Rev. B: Condens. Matter Mater. Phys.* **2004**, *70*, 195327.
(45) Nienhaus, L.; Dustin, D. E.; Xue, Z.; Moore, J. S.; Gruebele, M. *J. Photochem. Photobiol., A* **2014**, *295*, 26.
(46) Kang, I.; Wise, F. W. *J. Opt. Soc. Am. B* **1997**, *14*, 1632.
(47) Bragas, A. V.; Landi, S. M.; Martínez, O. E. *Appl. Phys. Lett.* **1998**, *72*, 2075.
(48) Pijpers, J. J. H.; Ulbricht, R.; Tielrooij, K. J.; Osherov, A.; Golan, Y.; Delerue, C.; Allan, G.; Bonn, M. *Nat. Phys.* **2009**, *5*, 811.
(49) Ellingson, R. J.; Beard, M. C.; Johnson, J. C.; Yu, P.; Micic, O. I.; Nozik, A. J.; Shabaev, A.; Efros, A. L. *Nano Lett.* **2005**, *5*, 865.
(50) Fernée, M. J.; Watt, A.; Warner, J.; Heckenberg, N.; Rubinsztein-Dunlop, H. *Nanotechnology* **2004**, *15*, 1328.
(51) Carmichael, E. S.; Gruebele, M. *J. Phys. Chem. C* **2009**, *113*, 4495.
(52) Frisch, M. J.; Trucks, G. W.; Schlegel, H. B.; Scuseria, G. E.; Robb, M. A.; Cheeseman, J. R.; Scalmani, G.; Barone, V.; Mennucci, B.; Petersson, G. A.; Nakatsuji, H.; Caricato, M.; Li, X.; Hratchian, H. P.; Izmaylov, A. F.; Bloino, J.; Zheng, G.; Sonnenberg, J. L.; Hada, M.; Ehara, M.; Toyota, K.; Fukuda, R.; Hasegawa, J.; Ishida, M.; Nakajima, T.; Honda, Y.; Kitao, O.; Nakai, H.; Vreven, T.; Montgomery, J. A., Jr.; Peralta, J. E.; Ogliaro, F.; Bearpark, M.; Heyd, J. J.; Brothers, E.; Kudin, K. N.; Staroverov, V. N.; Kobayashi, R.; Normand, J.; Raghavachari, K.; Rendell, A.; Burant, J. C.; Iyengar, S. S.; Tomasi, J.; Cossi, M.; Rega, N.; Millam, J. M.; Klene, M.; Knox, J. E.; Cross, J. B.; Bakken, V.; Adamo, C.; Jaramillo, J.; Gomperts, R.; Stratmann, R. E.; Yazyev, O.; Austin, A. J.; Cammi, R.; Pomelli, C.; Ochterski, J. W.; Martin, R. L.; Morokuma, K.; Zakrzewski, V. G.; Voth, G. A.; Salvador, P.; Dannenberg, J. J.; Dapprich, S.; Daniels, A. D.; Farkas, Ö.; Foresman, J. B.; Ortiz, J. V.; Cioslowski, J.; Fox, D. J. *Gaussian 09*; Gaussian, Inc.: Wallingford, CT, 2009.
(53) Perdew, J. P.; Burke, K.; Ernzerhof, M. *Phys. Rev. Lett.* **1996**, *77*, 3865.
(54) Perdew, J. P.; Burke, K.; Ernzerhof, M. *Phys. Rev. Lett.* **1997**, *78*, 1396.
(55) Hay, P. J.; Wadt, W. R. *J. Chem. Phys.* **1985**, *82*, 299.
(56) Hay, P. J.; Wadt, W. R. *J. Chem. Phys.* **1985**, *82*, 270.
(57) Wadt, W. R.; Hay, P. J. *J. Chem. Phys.* **1985**, *82*, 284.
(58) Check, C. E.; Faust, T. O.; Bailey, J. M.; Wright, B. J.; Gilbert, T. M.; Sunderlin, L. S. *J. Phys. Chem. A* **2001**, *105*, 8111.
(59) Kim, D.; Kim, D.-H.; Lee, J.-H.; Grossman, J. C. *Phys. Rev. Lett.* **2013**, *110*, 196802.
(60) Colvin, V. L.; Alivisatos, A. P. *J. Chem. Phys.* **1992**, *97*, 730.
(61) Möller, R.; Albrecht, U.; Boneberg, J.; Koslowski, B.; Leiderer, P.; Dransfeld, K. *J. Vac. Sci. Technol., B: Microelectron. Process. Phenom.* **1991**, *9*, 506.
(62) Lenner, M.; Rácz, P.; Dombi, P.; Farkas, G.; Kroó, N. *Phys. Rev. B: Condens. Matter Mater. Phys.* **2011**, *83*, 205428.
(63) Fracasso, D.; Valkenier, H.; Hummelen, J. C.; Solomon, G. C.; Chiechi, R. C. *J. Am. Chem. Soc.* **2011**, *133*, 9556.
(64) Krenner, H. J.; Sabathil, M.; Clark, E. C.; Kress, A.; Schuh, D.; Bichler, M.; Abstreiter, G.; Finley, J. J. *Phys. Rev. Lett.* **2005**, *94*, 057402.
(65) Koole, R.; Liljeroth, P.; de Mello Donegá, C.; Vanmaekelbergh, D.; Meijerink, A. *J. Am. Chem. Soc.* **2006**, *128*, 10436.
(66) Logar, M.; Xu, S.; Acharya, S.; Prinz, F. B. *Nano Lett.* **2015**, *15*, 1855.

DOI: 10.1021/jacs.5b09272
J. Am. Chem. Soc. 2015, 137, 14743−14750